

Precipitation of dopants on acceptor-doped $\text{LaMnO}_{3 \pm \delta}$ revealed by defect chemistry from first principles

Cite as: J. Chem. Phys. **154**, 064702 (2021); <https://doi.org/10.1063/5.0035691>

Submitted: 30 October 2020 . Accepted: 23 December 2020 . Published Online: 09 February 2021

 Franziska Hess, and  Bilge Yildiz

COLLECTIONS

Paper published as part of the special topic on [Special Collection in Honor of Women in Chemical Physics and Physical Chemistry](#)



View Online



Export Citation



CrossMark

ARTICLES YOU MAY BE INTERESTED IN

[r²SCAN-D4: Dispersion corrected meta-generalized gradient approximation for general chemical applications](#)

The Journal of Chemical Physics **154**, 061101 (2021); <https://doi.org/10.1063/5.0041008>

[Predicting the impact sensitivities of energetic materials through zone-center phonon up-pumping](#)

The Journal of Chemical Physics **154**, 064105 (2021); <https://doi.org/10.1063/5.0036927>

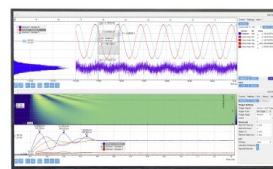
[r²SCAN-3c: A “Swiss army knife” composite electronic-structure method](#)

The Journal of Chemical Physics **154**, 064103 (2021); <https://doi.org/10.1063/5.0040021>



Challenge us.

What are your needs for
periodic signal detection?



Zurich
Instruments

Precipitation of dopants on acceptor-doped $\text{LaMnO}_{3\pm\delta}$ revealed by defect chemistry from first principles

Cite as: J. Chem. Phys. 154, 064702 (2021); doi: 10.1063/5.0035691

Submitted: 30 October 2020 • Accepted: 23 December 2020 •

Published Online: 9 February 2021



Franziska Hess^{1,2} and Bilge Yildiz^{1,3,a)}

AFFILIATIONS

¹Department of Nuclear Science and Engineering, Massachusetts Institute of Technology, 77 Massachusetts Avenue, Cambridge, Massachusetts 02139, USA

²Institute of Chemistry, Technical University Berlin, Strasse des 17. Juni 124, 10623 Berlin, Germany

³Department of Materials Science and Engineering, Massachusetts Institute of Technology, 77 Massachusetts Avenue, Cambridge, Massachusetts 02139, USA

Note: This paper is part of the JCP Special Collection in Honor of Women in Chemical Physics and Physical Chemistry.

a) Author to whom correspondence should be addressed: byildiz@mit.edu

ABSTRACT

Perovskite oxides degrade at elevated temperatures while precipitating dopant-rich particles on the surface. A knowledge-based improvement of surface stability requires a fundamental and quantitative understanding of the dopant precipitation mechanism on these materials. We propose that dopant precipitation is a consequence of the variation of dopant solubility between calcination and operating conditions in solid oxide fuel cells (SOFCs) and electrolyzer cells (SOECs). To study dopant precipitation, we use 20% (D = Ca, Sr, Ba)-doped $\text{LaMnO}_{3+\delta}$ (LDM20) as a model system. We employ a defect model taking input from density functional theory calculations. The defect model considers the equilibration of LDM20 with a reservoir consisting of dopant oxide (DO), peroxide (DO_2), and O_2 in the gas phase. The equilibrated non-stoichiometry of the A-site and B-site as a function of temperature, T , and oxygen partial pressure, $p(\text{O}_2)$, reveals three regimes for LDM20: A-site deficient (oxidizing conditions), A-site rich (atmospheric conditions), and near-stoichiometric (reducing conditions). Assuming an initial A/B non-stoichiometry, we compute the dopant precipitation boundaries in a p - T phase diagram. Our model predicts precipitation both under reducing (DO) and under highly oxidizing conditions (DO_2). We found precipitation under anodic, SOEC conditions to be promoted by large dopant size, while under cathodic, SOFC conditions precipitation is promoted by initial A-site excess. The main driving forces for precipitation are oxygen uptake by the condensed phase under oxidizing conditions and oxygen release assisted by B-site vacancies under reducing conditions. Possible strategies for mitigating dopant precipitation under in electrolytic and fuel cell conditions are discussed.

Published under license by AIP Publishing. <https://doi.org/10.1063/5.0035691>

I. INTRODUCTION

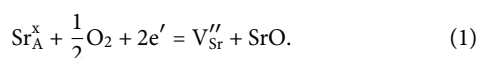
Perovskite oxides can accommodate a wide range of cation and anion nonstoichiometries,^{1–3} as well as cation substitution, which results in a complex defect chemistry. This makes them suitable for a wide variety of applications because their properties can be tuned easily. Their chemical and electrochemical applications range from heterogeneous catalysis^{4–6} and solar-to-fuels^{7–9} to oxide ion¹⁰ or proton conductors^{10,11} and electrode materials.^{5,12,13} With A and

B representing a large and a small cation, respectively, their general composition is expressed as ABO_3 .

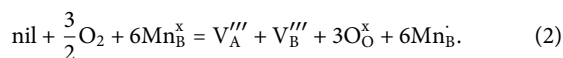
Being used in a variety of applications, they must be tolerant toward large changes of the reaction conditions, such as temperature, oxygen partial pressure, and impurity content (such as H_2O , CO_2 , and sulfur) in the gas phase. However, the enrichment of dopants close to the surface and the precipitation of secondary phases are frequently observed in perovskite-based oxygen electrodes in solid oxide fuel cells (SOFCs) and electrolyzer

cells (SOECs).^{13–19} Some perovskite oxide solid solutions can exhibit structural instabilities resulting in the decomposition of several perovskite phases with different compositions.²⁰ Changes in the surface structure and compositions are also observed in room-temperature electrochemical applications.²¹ Such dopant enrichment has been correlated with a drop in surface oxygen exchange activity in many cases,^{22–24} although the origin and generality of such observations is still debated.^{25–28} The enrichment of dopants near the surface has recently been explained by a density functional theory (DFT)-based *ab initio* thermodynamics model of $\text{La}_{0.75}\text{Sr}_{0.25}\text{MnO}_3$ (LSM25) in our recent work.²⁹ We demonstrated that the surface free energy under SOFC operating conditions is minimized by a surface configuration with oxygen vacancies, whose positive relative charge is balanced by enriched dopants of relative negative charge, still within the perovskite surface lattice. Dopant-rich phase precipitation, on the other hand, was predicted to occur only under SOEC operating conditions (anodic polarization), but not under SOFC operating conditions (cathodic polarization). This result conflicts with our recent experimental results where precipitation is shown to occur reversibly under both SOEC and SOFC conditions for $\text{La}_{0.8}\text{Ca}_{0.2}\text{MnO}_3$ (LCM20), $\text{La}_{0.8}\text{Sr}_{0.2}\text{MnO}_3$ (LSM20), and $\text{La}_{0.8}\text{Ba}_{0.2}\text{MnO}_3$ (LBM20).³⁰ To resolve this discrepancy, we propose that dopant precipitation from doped perovskites is not a pure surface phenomenon; rather, changes in the bulk defect chemistry with temperature, oxygen pressure, and electrochemical polarization can also contribute to causing dopant phase precipitation. To examine this hypothesis, we extend the established defect model for $\text{La}_{1-x}\text{Sr}_x\text{MnO}_{3+\delta}$ ^{31,32} and Nb-doped SrTiO_3 ³³ to account for the equilibration of the A-site sublattice with a dopant oxide reservoir.

The precipitation of SrO from La- and Nb-doped SrTiO_3 has previously been examined in the literature using an experiment-based defect chemistry model.³³ Therein, the precipitation of SrO under atmospheric conditions is explained as an oxidation process forming cation vacancies,³³



Equation (1) is not energetically favored in doped lanthanum manganites (*vide infra*), in general. Instead, the dominant oxygen uptake process is described as a Schottky reaction forming A-site and B-site vacancies in equal proportion without phase precipitation,³¹



Here, nil indicates an empty perovskite unit cell. We propose that incorporating Eq. (1) into the defect chemistry model together with Eq. (2) is able to predict the equilibrium A/B ratio in the perovskite as a function of temperature and $p(\text{O}_2)$ and finally that dopant precipitation in the form of an oxide or peroxide can be explained by a decrease in the thermodynamically stable A/B ratio under SOEC/SOFC operating conditions compared to typical calcination conditions.

Acceptor-doped perovskite oxides used as solid oxide cell electrodes, such as $\text{La}_{1-x}\text{Sr}_x\text{MnO}_{3+\delta}$, $\text{La}_{1-x}\text{Sr}_x\text{CoO}_{3+\delta}$, or $\text{La}_{1-x}\text{Sr}_x\text{FeO}_{3+\delta}$, are usually nonstoichiometric.^{31,34–39} While the

oxygen nonstoichiometry of these materials has been studied in detail (both experimentally^{31,34–38,40–45} and computationally³²) and is well-understood, perovskite oxides can also exhibit an A/B nonstoichiometry. For instance, an A-site deficiency of several percent in $\text{La}_{0.8}\text{Sr}_{0.2}\text{MnO}_3$ used for fuel cell cathodes improves cathode durability by suppressing chemical reactions, such as the formation of $\text{La}_2\text{Zr}_2\text{O}_7$, between the electrode and the electrolyte.⁴⁶ A-site deficiency is also exploited in the exsolution of B-site dopants as metallic nanoparticles in perovskite oxides^{47,48} that exhibit enhanced properties in catalysis^{49,50} and electrocatalysis.^{48,51,52} So far, there is only a basic understanding of the extent of A/B nonstoichiometry (phase width), how it relates to the dopant size, temperature, and oxygen partial pressure, and how it affects the material performance and properties. According to x-ray diffraction studies, the A-site deficiency of 20% Sr- and Ca-substituted LaMnO_3 in air can be as high as 5%⁵³ or 10%⁴⁶ and up to 10% in pure LaMnO_3 .^{53,54} While it is currently unknown whether or not B-site deficient acceptor-doped LaMnO_3 powders are stable or not, the extent of B-site deficiency has been reported and quantified for other perovskites, such as pure $\text{LaMn}_{1-y}\text{O}_3$ (3%,⁵⁵ 6%⁵⁶), $(\text{Ba}_{0.5}\text{Sr}_{0.5})(\text{Co}_{0.8}\text{Fe}_{0.2})_{1-y}\text{O}_3$ (8%),⁵⁷ $\text{Sr}_{0.9}\text{La}_{0.1}\text{Ti}_{1-y}\text{O}_3$ (6%),⁵⁸ $\text{Y}_{0.08}\text{Sr}_{0.92}\text{Ti}_{1-y}\text{O}_3$ (5%),⁵⁹ $\text{Pr}_{0.5}\text{Ba}_{0.5}\text{Co}_{1-y}\text{O}_3$ (>10%),⁶⁰ $\text{La}_{0.5}\text{Sr}_{0.5}\text{Co}_{1-y}\text{O}_3$ (0.3%),⁶¹ and $\text{La}_{0.85}\text{Sr}_{0.15}\text{Co}_{1-y}\text{O}_3$ (>2%).⁶² B-site deficiency has also been reported for thin films of SrTiO_3 ^{63–66} and $\text{La}_{0.8}\text{Ba}_{0.2}\text{MnO}_3$.⁶⁷ Based on these data, we assume that acceptor-doped LaMnO_3 can support both A-site and B-site deficiency.

In this contribution, we revisit the defect chemistry of 20% (Ca, Sr, Ba)-doped lanthanum manganites $(\text{La}_{0.8}\text{D}_{0.2})_{1+y}\text{MnO}_{3+\delta}$ (LCM20, LSM20, LBM20) by a new defect model, employing defect formation energies and entropies computed by Density Functional Theory (DFT). We extend the established lanthanum manganite defect chemistry model by enabling the equilibration of both the oxygen sublattice and the A-site cation sublattice with external reservoirs. In doing so, we elucidate the driving forces of the precipitation of dopant oxides and how it depends on T and $p(\text{O}_2)$. The dopant oxide reservoir consists of dopant oxide (DO) and peroxide (DO_2) equilibrated with O_2 . The dopant oxide/peroxide reservoir will be denoted as DO_x , representing the equilibrated and DO/DO_2 mixture present in infinite amount. This is an open system problem that can be imagined as a composite of LCM20 and an excess of DO_x , enabling both the dopant uptake by and release from the perovskite lattice. We compute the equilibrium A/B nonstoichiometry as a function of temperature, T , and effective oxygen pressure, $p(\text{O}_2)$. As a result, we identify three regimes where equilibrated LCM20 is near-stoichiometric under reducing conditions, A-site rich under atmospheric and oxidizing conditions, and A-site depleted under strongly oxidizing conditions. Assuming an initial A/B nonstoichiometry, we compute the precipitation phase boundaries of DO_x in a p - T diagram. Our model predicts the precipitation of DO under reducing and of DO_2 under highly oxidizing conditions. DO formation under reducing conditions is highly sensitive to the initial A/B non-stoichiometry. DO_2 , however, precipitates under highly oxidizing conditions, regardless of the initial A/B nonstoichiometry. Under strongly oxidizing conditions, the precipitation onsets of the three dopants vary significantly because the binding energy of the dopant depends on its size within the perovskite lattice. We

note that surfaces do not exist explicitly in this model. Dopant precipitates usually emerge on the surfaces of perovskite oxides. However, our model presents evidence that the cause of dopant precipitation does not have to be surface instability alone, but that point defect thermodynamics within the perovskite oxide bulk can also play a significant role. Based on these findings, we discuss possible strategies to improve electrode durability for SOEC and SOFC functions.

II. COMPUTATIONAL DETAILS

To study the dopant precipitation from acceptor-doped LaMnO_3 , we employ a density functional theory (DFT)-based thermodynamics and defect chemistry approach. We extend the established defect model for acceptor-doped LaMnO_3 by an additional defect reaction that accounts for the exchange of cations between the perovskite and the DO_x reservoir. The energetics of defect reactions and formation energies of precipitates are computed using PBE+U. Entropies of defect reactions and precipitation are estimated from vibrational frequency calculations.

A. Density functional theory calculations

The density functional theory (DFT) calculations were performed using the Vienna *Ab initio* Simulation Package (VASP)^{68,69} using the Perdew–Burke–Ernzerhof (PBE) functional⁷⁰ with a Hubbard-U correction⁷¹ of 4 eV on the Mn 3d orbital.¹⁵ Doped lanthanum manganites can exhibit a wide variety of magnetic properties, which varies with the dopant content. While pure LaMnO_3 assumes an antiferromagnetic ground state, ferromagnetism has been observed for $\text{La}_{1-x}\text{Sr}_x\text{MnO}_3$ for $0.16 \leq x \leq 0.48$.⁷² Ferromagnetic spin ordering therefore best represents the ground state of $\text{La}_{0.8}\text{Sr}_{0.2}\text{MnO}_3$. An initial magnetic moment of 3.5 on Mn was sufficient to reliably converge the calculations into the ferromagnetic, half-metallic state. For bulk computations, meshes of $(6 \times 6 \times 4)$ k-points were chosen for the primitive orthorhombic cells [corresponding to $(\sqrt{2} \times \sqrt{2} \times 2)$ super cells of the pseudocubic perovskite structure]. Due to their small size, these primitive cells were not employed in the calculations of defect properties and entropies (*vide infra*). Together with an energy cutoff of 550 eV, this approach ensures convergence of total energies and bulk vacancy formation energies within 4 meV/atom. An overbinding correction⁷³ of +1.03 eV was applied to the O_2 molecule, resulting in a total energy of O_2 of −8.838 eV.

Based on neutron diffraction studies of LaMnO_3 (LMO), doped lanthanum manganites have been proposed to assume a cubic structure above 750 K; however, LaMnO_3 retains its orthorhombic symmetry despite the transition to a metrically cubic lattice (Ref. 74 and references therein). The apparently cubic structure has been proposed to be a result of dynamic fluctuations. We assume the same to be the case for our model system, LaMnO_3 doped with 20% Ca, Sr, and Ba ($\text{La}_{0.8}\text{D}_{0.2}\text{MnO}_3$, with D = Ca, Sr, Ba, i.e., LCM20, LSM20, and LBM20). All our bulk calculations are performed in a symmetry-free configuration with orthorhombic (*Pnma*) atom positions as a starting guess. The structure is allowed to freely relax without symmetry constraints, however, so that the relaxed structure may deviate substantially from orthorhombic symmetry for high vacancy concentrations.

Defect energies in the mixed oxide bulk were calculated in a 64-unit $(4 \times 4 \times 4)$ supercell with the composition $\text{La}_{51}\text{D}_{13}\text{Mn}_{64}\text{O}_{192}$ with random arrangements of dopant cations and defects and orthorhombic starting positions. The k-mesh was scaled to the large super cells according to standard practice, resulting in $(2 \times 2 \times 2)$ k-points for the 320-atom unit cell. For each defect energy, four random configurations were computed and averaged. The statistical error of defect reactions energies was estimated from the scatter between individual defect calculations, which is ± 0.15 eV.

Normal modes of vibration in doped LaMnO_3 were computed in 8-unit $(2 \times 2 \times 2)$ supercells using the finite displacement method with a displacement of 0.015 Å, resulting in $3N - 3$ real vibrational modes, with N being the number of atoms in the supercell. A k-mesh with $(4 \times 4 \times 4)$ points was used in these calculations.

B. *Ab initio* thermochemistry

The model requires five equilibrium constants, K_{ox} , K_{red} , K_{disp} , K_{prec} , and $K_{\text{DO}/\text{DO}_2}$, associated with reactions described in Eqs. (8)–(12) below. The equilibrium constant can be computed from the standard Gibbs energy of reaction as a function of temperature,

$$\log(K(T)) = -\frac{\Delta_r G(T)}{k_B T}. \quad (3)$$

The standard Gibbs energy of the defect reactions is estimated from DFT-calculated reaction energies ΔE at 0 K as

$$\Delta_r G(T) \approx \Delta E - T \Delta_r S. \quad (4)$$

All entropy contributions were estimated from DFT vibrational calculations and statistical thermodynamics.

We assume vibrational reaction entropies to be independent of the defect concentration. Hence, the vibrational reaction entropy of reaction i only depends on how much oxygen (Δn_O) and dopant (Δn_D) are exchanged between solid phases and the gas phase,

$$\Delta_r S_i = \Delta n_{O,i} \left(\frac{1}{2} \cdot S_{\text{O}_2, \text{gas}} - \Delta S_{\text{O}, \text{lat}} \right) + \Delta n_{D,i} \cdot (S_{\text{DO}} - \Delta S_{D, \text{lat}}). \quad (5)$$

$\Delta S_{D, \text{lat}}$ and $\Delta S_{\text{O}, \text{lat}}$ indicate the change in vibrational entropy at 298 K upon removal of a dopant or oxygen atom from the lattice. It is computed as the entropy difference between a supercell with an A-site or oxygen vacancy and a perfect super cell, for instance,

$$\Delta S_{D, \text{lat}} = S_{\text{LDM}, \text{perfect}} - S_{\text{LDM}, V_A'''} \quad (6)$$

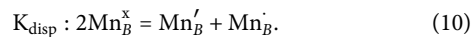
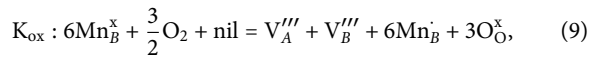
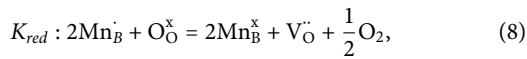
The entropies were calculated from the energies of the normal modes of vibration using statistical thermodynamics,

$$\frac{S_j}{R} = \sum_{i=1}^{3N_j-3} \frac{\varepsilon_{ij}}{k_B T} \cdot \left(e^{\frac{\varepsilon_{ij}}{k_B T}} - 1 \right)^{-1} - \ln \left(1 - e^{-\frac{\varepsilon_{ij}}{k_B T}} \right), \quad (7)$$

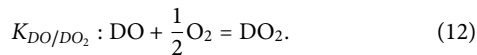
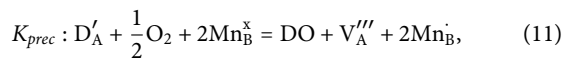
where ε_{ij} denotes the energy of the i th vibrational mode in configuration j , T is temperature, and k_B and R denote the Boltzmann and ideal gas constants.

III. EXTENSION OF THE DEFECT MODEL FOR ACCEPTOR-DOPED LaMnO_3

Our defect computations are methodologically similar to a previous DFT-based study by Lee and Morgan.³² In addition to the precipitation equilibrium [Eq. (8)], we consider reduction of LDM (forming oxygen vacancies), oxidation (forming cation vacancies), and charge disproportionation, as described in the following reactions:



To account for the exchange of the dopant cations D'_A with the environment, we need to consider the equilibration of the A-site cation sublattice with an external dopant cation reservoir. We model this reservoir as a mixture of DO and DO_2 , which is equilibrated with the gas phase,



Since the last equilibrium [Eq. (12)] only depends on the oxygen chemical potential, the activities of DO (a_{DO}) and DO_2 (a_{DO_2}) can be determined independently of the defect equilibria of LSM. Frequently, the activities of pure solid compounds are assumed as 1 by convention. However, this convention is not applicable in the present case as explained in detail in Note S1 in the [supplementary material](#). Defining $1 = a_{\text{DO}} + a_{\text{DO}_2}$, the DO/ DO_2 equilibrium constant, $K_{\text{DO/DO}_2}$, and the activity of the dopant oxide, a_{DO} , can be written as

$$K_{\text{DO/DO}_2} = \frac{a_{\text{DO}_2} \cdot p_0^{1/2}}{a_{\text{DO}} \cdot p_{\text{O}_2}^{1/2}} = \frac{(1 - a_{\text{DO}})}{a_{\text{DO}} \cdot \left(\frac{p_{\text{O}_2}}{p_0}\right)^{1/2}}, \quad (13)$$

$$a_{\text{DO}} = \frac{1}{K_{\text{DO/DO}_2} \cdot \left(\frac{p_{\text{O}_2}}{p_0}\right)^{1/2} + 1}. \quad (14)$$

The equilibrium constant of the precipitation reaction [Eq. (11)] can then be written as

$$K_{\text{prec}} = \frac{a_{\text{DO}} \cdot [\text{V}_A^{\cdot\cdot\cdot}] \cdot [\text{Mn}_B^{\cdot}]^2 \cdot p_0^{1/2}}{[\text{D}'_A] \cdot [\text{Mn}_B^{\times}]^2 \cdot p_{\text{O}_2}^{1/2}}, \quad (15)$$

$$K_{\text{prec}} = \frac{1}{\left(K_{\text{DO/DO}_2} \cdot p_{\text{O}_2}^{1/2} + 1\right)} \cdot \frac{[\text{V}_A^{\cdot\cdot\cdot}] \cdot [\text{Mn}_B^{\cdot}]^2 \cdot p_0^{1/2}}{[\text{D}'_A] \cdot [\text{Mn}_B^{\times}]^2 \cdot p_{\text{O}_2}^{1/2}}. \quad (16)$$

The laws of mass action for reactions (8)–(10) and the required balance equations are given in Sec. III. In addition to the site and charge balances, we need additional balances to account for the initial A/B ratio, the initial dopant concentration, and the amount of Sr that is exchanged with the reservoir. The initial A/B ratio is given by a constant $\delta_{AB,0}$, which is equal to the difference between the initial (indicated by an index 0) total B-site and A-site occupations,

$$\delta_{AB,0} = [\text{Mn}_B^{\cdot}]_0 + [\text{Mn}_B^{\times}]_0 + [\text{Mn}_B^{\cdot}]_0 - [\text{D}'_A]_0 - [\text{La}_A^{\times}]_0. \quad (17)$$

The initial dopant concentration, $x_{D,0}$, defines the initial ratio of $[\text{D}'_A]_0/[\text{La}_A^{\times}]_0$,

$$\frac{[\text{La}_A^{\times}]_0}{[\text{D}'_A]_0} = 1 - x_{D,0}. \quad (18)$$

The sum of $[\text{La}_A^{\times}] + [\text{D}'_A]$ is not necessarily equal to 1 because the formation of cation vacancies is possible and the number of A-site vacancies can be affected by dopant exchange between the perovskite and the reservoir. δ_D indicates the change in the dopant site fraction,

$$\frac{[\text{La}_A^{\times}]}{[\text{D}'_A] - \delta_D} = 1 - x_{D,0}, \quad (19)$$

i.e., a positive and negative δ_D indicate precipitation and dissolution, respectively. Due to dopant precipitation, the number of A-site vacancies changes,

$$[\text{V}_A^{\cdot\cdot\cdot}] = [\text{V}_B^{\cdot\cdot\cdot}] - \delta_{AB,0} + \delta_D. \quad (20)$$

The resulting equations (19) and (20) are new balance equations not considered in previous defect chemistry models of LSM. $x_{D,0}$ and $\delta_{AB,0}$ are parameters defining initial material properties, while δ_D is one of the unknown parameters obtained from the final solution of the equation system.

The laws of mass action and balance equation together form a system of ten linearly independent equations,

$$\text{A - site balance} \quad 1 = [\text{La}_A^{\times}] + [\text{D}'_A] + [\text{V}_A^{\cdot\cdot\cdot}], \quad (21)$$

$$\text{B - site balance} \quad 1 = [\text{Mn}_B^{\times}] + [\text{Mn}_B^{\cdot}] + [\text{Mn}_B^{\cdot}] + [\text{V}_B^{\cdot\cdot\cdot}], \quad (22)$$

$$\text{O - site balance} \quad 3 = [\text{O}_O^{\times}] + [\text{V}_O^{\cdot\cdot}], \quad (23)$$

$$\text{charge balance} \quad 0 = -[\text{D}'_A] - 3[\text{V}_A^{\cdot\cdot\cdot}] - 3[\text{V}_B^{\cdot\cdot\cdot}] + [\text{Mn}_B^{\cdot}] - [\text{Mn}_B^{\cdot}] + 2[\text{V}_O^{\cdot\cdot}], \quad (24)$$

$$\text{dopant balance} \quad \frac{[\text{La}_A^{\times}]}{[\text{D}'_A] - \delta_D} = 1 - x_{D,0}, \quad (25)$$

$$\text{vacancy balance} \quad [V_A'''] = [V_B'''] - \delta_{AB,0} + \delta_D, \quad (26)$$

$$\text{reduction} \quad K_{red} = \frac{p_{O_2}^{1/2} \cdot [V_O^\cdot] \cdot [Mn_B^x]^2}{p_0^{1/2} \cdot [O_O^x] \cdot [Mn_B^\cdot]^2}, \quad (27)$$

$$\text{oxidation} \quad K_{ox} = \frac{[O_O^x]^3 \cdot [V_A'''] \cdot [V_B'''] \cdot [Mn_B^\cdot]^6 \cdot p_0^{3/2}}{3^3 \cdot [Mn_B^\cdot]^6 \cdot p_{O_2}^{3/2}}, \quad (28)$$

$$\text{charge disproportionation} \quad K_{disp} = \frac{[Mn_B^\cdot] \cdot [Mn_B']}{[Mn_B^x]}, \quad (29)$$

precipitation

$$K_{prec} = \frac{[V_A'''] \cdot [Mn_{Mn}^\cdot]^2 \cdot p_0^{1/2}}{\left(K_{DO/DO_2} \cdot \left(\frac{p_{O_2}}{p_0}\right)^{1/2} + 1\right) \cdot [D_A'] \cdot [Mn_{Mn}^x]^2 \cdot p_{O_2}^{1/2}}. \quad (30)$$

This set of algebraic equations is solved to obtain the ten unknowns, $[La_A^x]$, $[D_A']$, $[V_A''']$, $[Mn_B^x]$, $[Mn_B^\cdot]$, $[Mn_B']$, $[V_B''']$, $[O_O^x]$, $[V_O^\cdot]$, and δ_D . Finally, this system of equations is solved numerically using Wolfram Mathematica. While there can potentially be many solutions for the ten unknowns, we found that there is only one physically sensible result which makes the solution unambiguous.

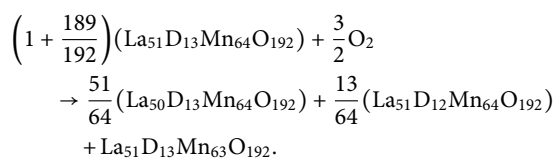
IV. RESULTS

A. Defect thermodynamics of LCM, LSM, and LBM

We employ density functional theory calculations to compute the reaction energies and entropies of the defect reactions and ultimately the equilibrium constants K_{red} , K_{ox} , and K_{prec} . Only K_{disp} was adopted from the study of Lee and Morgan on $LaMnO_3$ ³² and is assumed to be identical for all three dopants.

All defect computations were conducted in neutral 64-unit supercells, where ionic defects are compensated by opposing electronic defects. The reaction energies of some of these defect reactions, particularly the Schottky reaction, cannot be computed directly because removing several cations from the super cell would result in a large concentration of cation defects and also change the ratio between La and the dopant. We therefore compute the reaction energy as a sum of several super cells, each containing a different, isolated defect, while preserving the total number of La, dopant, Mn, and O atoms on the left- and right-hand side of the equation. This approach also allows us to keep the concentration of ionic defects in each super cell small.

For instance, to model the Schottky reaction, we compute



Each of the compositions on the right side represents a unit cell with a single cation vacancy with its compensating electronic defects (altogether 6 Mn[•]). Again, each of the compositions is represented by an average over four different configurations. This approach ensures that the overall ratio of La/dopant ≈ 4 is retained before and after oxidation and defect concentrations are kept low to minimize the interaction of defects with each other.

Our defect model includes entropy contributions for O_2 , lattice O, and dissolved dopants, as well as the precipitated oxides. We find that all entropy contributions matter in equilibrium. We note, in particular, that individual entropy contributions cannot be left out of the calculation due to compensation effects between the dissolved dopants, precipitated oxides, and gas phase O_2 . Therefore, ignoring some entropy contributions while including others will result in larger errors than ignoring entropy contributions altogether. In the present manuscript, we deem the inclusion of entropy necessary because the equilibrium between oxygen bound in solid-state phases and oxygen in the gas phase is governed by entropy. By extension, the equilibria between phases that contain different stoichiometries of oxygen (DO , DO_2) are also strongly influenced by entropy.

When entropy contributions are switched off, all the precipitation lines will undergo some shifts. In particular, we find that ignoring entropy contributions can cause larger errors at high temperatures. However, we find that the main conclusion, which is that precipitation will occur under both reducing and oxidizing conditions, is not altered by ignoring entropy. Including entropy thus simply makes the overall results more accurate quantitatively. A precipitation diagram calculated without entropy contributions in the solid-state phases is included in Fig. S7 in the [supplementary material](#). The precipitation lines are shifted by up to two orders of magnitude toward higher $p(O_2)$ compared to the case where all entropy contributions are included in the calculations.

The entropies for the considered earth alkali oxide and peroxide compounds, as well as gas phase oxygen, are listed in [Table I](#). The

TABLE I. Vibrational entropies of compounds and defects in LDM at 298 K, as calculated from DFT (this study) or obtained from experiment.⁷⁵ $\Delta S_{x,lat}$ indicates the change in the bulk entropy upon removal of an ion x by forming a vacancy in the compound lat .

Compound/defect	S (DFT) · (K mol/J)	S (expt.) · (K mol/J)
O_2 (gas)	...	22.5
$\Delta S_{O,LCM}$	30.3	...
$\Delta S_{O,LSM}$	21.7	...
$\Delta S_{O,LBM}$	22.2	...
$\Delta S_{Ca,LCM}$	8.2	...
$\Delta S_{Sr,LSM}$	22.8	...
$\Delta S_{Ba,LSM}$	17.7	...
CaO	40.87	38.10 ⁷⁵
SrO	55.27	55.58 ⁷⁵
BaO	72.53	72.00 ⁷⁵
CaO ₂	56.30	...
SrO ₂	70.25	...
BaO ₂	94.99	93.09 ⁷⁵

deviation between computed and experimental values is less than 3 J/(K mol) for CaO, SrO, BaO, and BaO₂. The entropies of CaO₂ and SrO₂ have so far not been determined reliably from experiments due to the irreversibility of the peroxide decomposition reaction [Eq. (12)] for these compounds. The entropies of defect reactions were estimated from the change in vibrational entropy of the perovskite upon formation of oxygen or cation vacancies, $\Delta S_{O,lat}$ and $\Delta S_{D,lat}$. These reflect the combined loss of three degrees of freedom per oxygen removed from the lattice and the shift of the phonon modes due to the formation of a vacancy. They are calculated from the total entropies of the perfect perovskite, S_{LDM} , and the perovskite with a vacancy, S_{LDM+V_j} [Eq. (6)]. The defect entropies are listed in Table I. The only other (computational) estimate available in the literature is for oxygen in pure LaMnO₃ ($\Delta S_{O,LaMnO_3}$) from the work of Lee and Morgan [22.5 J/(K mol)],³² which is virtually identical to our result.

While there are no other data to validate our entropy calculations, we note that both the oxide and peroxide entropies follow the clear trend (shown by both experimental and calculated entropies) that entropy increases with the mass of the heaviest ion. This trend is expected from statistical thermodynamics because the vibrational entropy increases with decreasing vibrational frequency and the vibrational frequency decreases with mass. However, our dopant entropies $\Delta S_{D,LDM}$ do not follow this trend. Rather, entropy increases going from Ca to Sr but then decreases again going from Sr to Ba. It is uncertain if the trends known for binary compounds are applicable to quaternary compounds, in particular, because the total entropy is mostly governed by the heaviest ion (La), and the change in entropy upon vacancy formation is very sensitive to the change in the heaviest ion's vibrational frequencies. Our observed trend is partially rationalized by projection of the eigenmodes of vibration on the (x, y, z) translation of the dopant cations. The dopant-projected and averaged vibrational frequencies are 171.6 cm⁻¹, 125.4 cm⁻¹, and 118.4 cm⁻¹ for Ca, Sr, and Ba, respectively. While vibrational frequencies follow the trend of the ion mass, the change in the vibrational frequency going from Sr to Ba is only 7 cm⁻¹, compared to 46.2 cm⁻¹ going from Ca to Sr. Judging by the trend of these vibrational frequencies alone, the entropy change upon removal of a dopant cation $\Delta S_{D,LDM}$ can be only slightly higher for LBM than for LSM. The overall mode softening, however, changes this trend, which leads to an overall reduction in $\Delta S_{Ba,LBM}$.

In principle, we could validate our computed vibrational frequencies using the experimental Raman spectra; however, the

vibrational modes relevant for entropy are below 200 cm⁻¹, which makes them inaccessible for typical Raman equipment, and no spectra in this range are available. Since we cannot conclude from the available data if our computed dopant removal entropies are correct (and $\Delta S_{Ba,LBM}$ is questionable in particular), we will provide the final precipitation diagrams for LBM20 recomputed for higher $\Delta S_{Ba,LBM}$ [40 J/(K mol)] in the [supplementary material](#) for comparison (cf. Sec. IV C).

The final reaction energies and entropies of all reactions are listed in Table II, and we observe trends that can be understood by considering the cation radius. Within the series of LCM20, LSM20, and LBM20, both the energy of reduction and the energy of oxidation decrease going from Ca to Ba. This means that LCM20 is the hardest to reduce (+3.261 eV) and the easiest to oxidize (-2.160 eV), while LBM20 is the easiest to reduce (+2.978 eV) and the hardest to oxidize (-2.022 eV). This behavior could, in principle, be directly correlated with experimental measurements of oxygen nonstoichiometry for the three compounds. Unfortunately, the respective data are currently available only for LSM20,³¹ but not for LCM20 and LBM20. However, this trend is also reflected in the trend of the pseudocubic lattice parameter, where smaller and larger lattice parameters indicate higher oxidizability and higher reducibility, respectively. For LCM20 and LSM20, pseudocubic lattice parameters of 3.876 Å⁷⁶ and 3.885 Å⁷⁶ were determined by x-ray diffraction. The lattice parameter of LBM20 lies between 3.887 Å (LBM15)⁷⁷ and 3.889 Å (LBM30).⁷⁷ The lattice parameter increases along the Ca, Sr, Ba series, which leads us to expect the highest oxidizability for LCM20 and the highest reducibility for LBM20. This correlation between the dopant size and redox chemistry is rationalized by considering the change in the Mn oxidation state upon reduction or oxidation and the size of the cation. Ba is the largest dopant considered (1.61 Å); therefore, oxidation (which causes chemical contraction of the manganite lattice) is less favorable than in the case of LCM20, which has the smallest dopant (1.34 Å). The ionic radius of Sr is in between (1.44 Å) and so is the energy of oxidation. Reduction, on the other hand, causes chemical expansion; therefore, it is more favored for the largest dopant (Ba) than for the smallest dopant (Ca). This trend is not sustained for precipitation, where Sr in LSM20 has the highest precipitation energy (+0.524 eV) and Ca in LCM20 has the lowest (+0.141 eV). At first glance, this might suggest that LCM20 will show the most precipitation and LSM20 the least; however, this simple interpretation is false because precipitation also depends on the concentrations of Mn_B^x and Mn_B^y, which are strongly dependent on the oxygen

TABLE II. Reaction energies (0 K) and entropies (298 K) employed in the calculation of equilibrium constants.

	ΔE (eV)			$\Delta_r S$ (K/meV)		
	LCM20	LSM20	LBM20	LCM20	LSM20	LBM20
K_{red} [Eq. (27)]	+3.261	+3.110	+2.978	0.748	0.837	0.832
K_{ox} [Eq. (28)]	-2.160	-2.090	-2.022	-2.245	-2.512	-2.497
K_{disp} [Eq. (29)]	+0.06	+0.06	+0.06	0	0	0
K_{prec} [Eq. (30)]	+0.141	+0.524	+0.312	-0.724	-0.726	-0.494
K_{DO/DO_2} [Eq. (13)]	-0.543	-0.841	-1.123	-0.902	-0.907	-0.830

nonstoichiometry, δ_O . Drawing firm conclusions therefore requires solving all the defect equilibria simultaneously, and Eq. (30) alone does not explain precipitation under all reaction conditions, as will be shown later.

The oxide-peroxide reaction energies, on the other hand, are quite straightforward again. The result of solving the oxide/peroxide equilibrium is shown in Fig. S1 in the [supplementary material](#) for the three dopants. Red and blue areas in the figures represent the stability regions of the dopant oxide and peroxide, respectively. The relative stabilities of the earth alkali peroxides in air follow the sequence $\text{BaO}_2 > \text{SrO}_2 > \text{CaO}_2$, which is in excellent agreement with experimental decomposition temperatures.

B. A/B nonstoichiometry of the equilibrated material

The defect equilibria given in Sec. III were solved as a function of temperature and $p(\text{O}_2)$ over a large range of effective $p(\text{O}_2)$ [10^{-16} bar $\leq p(\text{O}_2) \leq 10^{16}$ bar]. The dopant oxide activities in the DO/DO₂ reservoirs were computed using Eq. (14). The results are shown in Fig. S1 in the [supplementary material](#). For comparison with experiments, we computed the oxygen nonstoichiometry (δ_O) for a model without equilibration of the Sr concentration and plotted the result together with experimental data by Mizusaki *et al.*³¹ in Fig. S2. The comparison shows very good agreement between the experimental and our calculated data for the reducing range of $p(\text{O}_2)$. For the oxidizing range, the agreement is not as good because our model neglects the repulsion between cation vacancies, which has been shown by Lee and Morgan to improve the agreement with experiment in the oxidizing range substantially.³² An overview of defect concentrations in both models is also shown in Fig. S2.

Our model assumes that both the O and A-site cation sublattices are equilibrated with external reservoirs. The equilibrated material can have both an oxygen and an A/B nonstoichiometry. We compute the A/B ratio and oxygen nonstoichiometry as

$$\delta_{AB} = \frac{1 - [V_A''']}{1 - [V_B''']} - 1, \quad (31)$$

$$\delta_O = \frac{3 - [V_O^{\bullet}]}{1 - \frac{1}{2}([V_A'''] + [V_B'''])} - 3. \quad (32)$$

The equilibrated A/B (δ_{AB}) and oxygen (δ_O) nonstoichiometries obtained from our defect model for LSM are shown in Figs. 1(a) and 1(b), respectively. A comparison of the resulting A/B nonstoichiometries for LCM20, LSM20, and LBM20 is shown in Fig. 2. The other defect concentrations are shown for LSM20 in Fig. 3. Because we observe no qualitative differences in the results between the three materials, only LSM20 will be discussed in detail below. The corresponding defect concentration data for LCM and LBM are shown in Fig. S3 in the [supplementary material](#).

For the equilibrated δ_{AB} in LSM20, we observe that the material is near-stoichiometric only under reducing conditions (white area). In this range, δ_{AB} is close to 0 but remains greater than 0 (A-site rich). LSM20 prefers to be slightly A-site rich (≈ 0.01 ppb = 10^{-11})

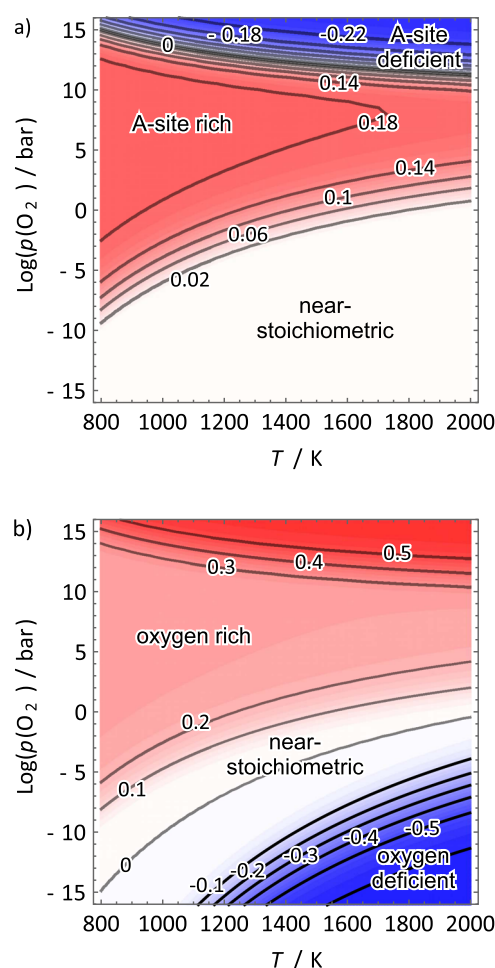


FIG. 1. Equilibrated A/B (δ_{AB}) nonstoichiometry in (a) and oxygen (δ_O) nonstoichiometry in (b) of LSM20 as a function of T and $p(\text{O}_2)$. Lines indicate isostoichiometry. Sign of nonstoichiometry is shown by colors: (a) blue: $\delta_{AB} < 0$ (A-site deficient), white: $\delta_{AB} \approx 0$ (A/B stoichiometric), and red: $\delta_{AB} > 1$ (A-site rich); (b) blue: $\delta_O < 0$ (oxygen-deficient), white: $\delta_O \approx 0$ (oxygen-stoichiometric), and red: $\delta_O > 0$ (oxygen-rich).

after equilibration. For LCM20 and LBM20, there is a slightly A-site deficient region under very reducing conditions [cf. Figs. 2(a) and 2(c)], but since δ_{AB} is within ± 0.01 ppb, this result is of no practical consequence. We consider this regime as near-stoichiometric for all three compounds and emphasize that these materials thermodynamically prefer to be A/B stoichiometric at high T and low $p(\text{O}_2)$. It will be shown in Sec. IV C that this behavior is the primary cause for dopant precipitation under reducing reaction conditions. The area of the near-stoichiometric A/B ratio covers both the oxygen-deficient regime under reducing conditions [red area in Fig. 1(a)] and the oxygen-stoichiometric regime [white area in Fig. 1(b)]. The reducing regime is characterized by the high oxygen vacancy concentration [blue curve in Fig. 3(a)] and high Mn^{2+} concentration [blue curve in Fig. 3(b)].

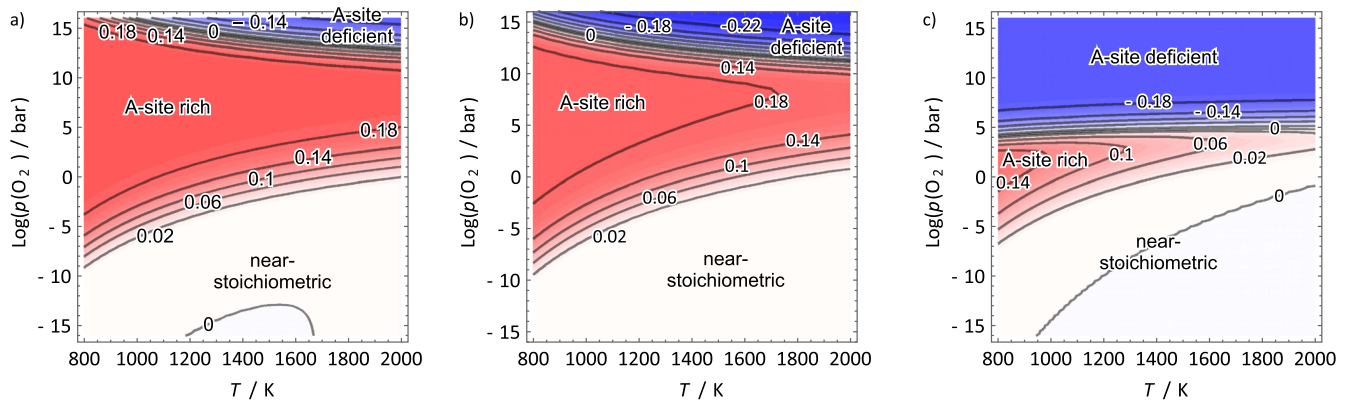
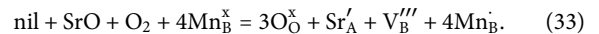


FIG. 2. Equilibrated A/B nonstoichiometries δ_{AB} for LCM20 (a), LSM20 (b), and LBM20 (c). Lines indicate constant nonstoichiometry. Sign of nonstoichiometry is shown by colors: blue—A-site deficient, white—near-stoichiometric, and red—A-site rich.

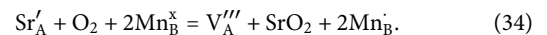
A-site excess ($\leq 20\%$) is obtained under atmospheric and oxidizing conditions [red area in Fig. 1(a)]. In this area, LSM20 is oxygen-stoichiometric [red area in Fig. 1(b)] with a large number of B-site vacancies [green curve in Fig. 3(a)] and most Mn oxidized to Mn^{4+} [green curve in Fig. 3(b)]. The Sr incorporation behaves similar to

the oxidation reaction given in Eq. (9), but due to the simultaneous uptake of SrO together with O_2 , only B-site vacancies are formed,



This results in a ratio of $[V_A''']/[V_B''']$ of about 10^7 [orange and green curves in Fig. 3(a)]. Because the reaction requires the uptake of gaseous oxygen, it is entropically more favored at low temperatures. As a consequence, a larger A-site excess is incorporated at lower temperatures than at higher temperatures, and the width of the A-site rich region on the $p(\text{O}_2)$ scale decreases with temperature as evident from the shape of the red regions for all three materials in Fig. 2. This is qualitatively in good agreement with the experimental findings by van Roosmalen *et al.* who reported that the range of stable A/B nonstoichiometries of pure LaMnO_3 decreases with temperature.⁵⁵ The size of the red area where A-site excess can be incorporated differs between the three materials (Fig. 2), with LCM [Fig. 2(a)] and LBM [Fig. 2(c)] having the largest and smallest stability ranges, respectively.

Under highly oxidizing conditions, an A-site deficient regime is identified [blue area in Fig. 1(a)]. It will be shown in Sec. IV C that SrO_2 precipitation occurs in this range, which can be described by the equation



It results in a large A-site deficit, as also observed by $[V_A''']$ [orange curve in Fig. 3(a)] overtaking $[V_B''']$ [green curve in Fig. 3(a)] at high $p(\text{O}_2)$. Both $[V_A''']$ and $[V_B''']$ are in the percent range, resulting in further increase in the oxygen excess [deep red region in Fig. 1(b)] up to 3.5. The transition between the A-site-rich and the A-site-deficient regime moves to lower $p(\text{O}_2)$ along the L(C, S, B)M series (Fig. 2).

C. Dopant precipitation

We showed in Sec. IV B that the equilibrated A/B nonstoichiometry is a function of T and $p(\text{O}_2)$ and can vary between -0.22 and 0.18 within the studied T - and $p(\text{O}_2)$ range. We propose that

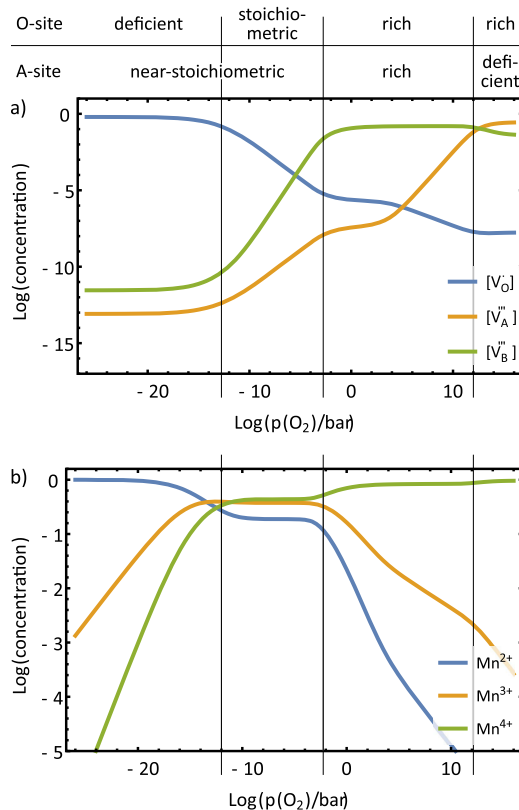
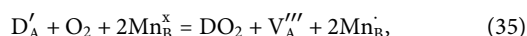


FIG. 3. Equilibrated defect concentrations in LSM20 at 1273 K. Nonstoichiometries for the A-site and O-site are indicated at the top. (a) Ionic defects $[V_O]$, $[V_A''']$, and $[V_B''']$. (b) Electronic defects $[\text{Mn}_B^{2+}]$ (Mn^{2+}), $[\text{Mn}_B^{3+}]$ (Mn^{3+}), $[\text{Mn}_B^{4+}]$ (Mn^{4+}).

an initial A-site excess in the sample can lead to precipitation upon annealing or during device operation if the equilibrium A/B ratio is exceeded at the given T and $p(\text{O}_2)$. We study dopant precipitation for A/B-nonstoichiometric starting materials by solving the defect equilibria given in Sec. III for an initial A-excess (δ_{AB}) in the range of $10^{-8} \leq \delta_{AB} \leq 10^{-2}$ for LCM20, LSM20, and LBM20. The resulting phase precipitation is indicated in Fig. 4. Each diagram can be divided into three zones, where there is either no precipitation, or earth alkali oxide, or peroxide precipitation. The zone without precipitation is located in the center of each diagram. The onsets of oxide precipitation (marked by red lines) are observed under reducing conditions and peroxide precipitation (marked by a blue line) under oxidizing conditions, respectively.

The different dopants, Ca, Sr, and Ba, show noticeable differences. The zone without precipitation is the largest for LCM20 and the smallest for LBM20, indicating that LCM20 is the most stable of three compounds and LBM20 is the least stable.

Under highly oxidizing conditions, the peroxide precipitation line shifts to lower $p(\text{O}_2)$ from Ca to Sr, to Ba. This means that among the three materials, LCM is expected to be the most stable under oxidizing conditions (or anodic polarization as in SOEC), while under reducing conditions (or cathodic polarization as in SOFC), all three materials may have similar instability. The precipitation of peroxide under oxidizing conditions occurs regardless of the initial A/B ratio of the material, and the location of the phase boundary is not influenced by δ_{AB} . It is explained by the peroxide precipitation reaction,



where O_2 appears as a reactant on the left-hand side of the equation. This reaction is driven by the high oxygen chemical potential under oxidizing conditions. The formation of SrO_2 upon precipitation has already been debated based on thermodynamical considerations;⁷⁸ SrO_2 has been identified as the precipitation product during $^{18}\text{O}_2$ exchange experiments on $(\text{La}_{0.75}\text{Sr}_{0.25})_2\text{CoO}_4$ and $(\text{La}_{0.5}\text{Sr}_{0.5})_2\text{CoO}_4$ at temperatures below 775 K.⁷⁹ Previous

thermodynamic considerations are based on the decomposition temperature of SrO_2 in air, which is around 800 K, in good agreement with our calculations (cf. Fig. S1). Based on the decomposition temperature alone, we would not expect the formation of SrO_2 at higher temperatures; however, under anodic polarization, the oxygen chemical potential increases proportional to the applied voltage, which shifts the decomposition to higher temperatures. As a result, SrO_2 can be formed by precipitation even under operating temperatures of an SOEC device (1000 K–1300 K) as shown by our calculations (Fig. S1 and Fig. 4). SrO_2 will decompose if anodic polarization is ceased at operating temperature, resulting in the detection of SrO [$\text{Sr}(\text{OH})_2$ or SrCO_3 in the presence of H_2O or CO_2 contaminants] in *post-mortem* characterization. Therefore, the absence of SrO_2 as a precipitate in high-temperature SOEC experiments does not contradict our modeling results.

We note that the peroxide precipitation reaction in the Ca, Sr, Ba series does not follow the exact energetic sequence of the precipitation equilibrium [Eq. (30)], which suggests that LCM20 should be the least stable and LSM20 should be the most stable. Instead, we find LCM20 the most and LBM20 the least stable. The observed trend is instead governed by different stabilities of the peroxides, which gives precipitation energies for Eq. (35) of -0.402 eV, -0.317 eV, and -0.815 eV for LCM20, LSM20, and LBM20, respectively, which is consistent with LBM20 being the least stable and LCM20 and LSM20 having similar stabilities in Fig. 4. The higher stability of LCM20 compared to LSM20 is explained by LCM20 being more oxidizable, which is due to the substantially higher entropy of oxygen in LCM20 [30.3 J/(K mol)] compared to LSM20 [21.7 J/(K mol)].

We find that the precipitation line of DO_2 is not noticeably affected by initial A-site excess because all the blue lines are on top of each other in Fig. 4. Although, by simple intuition, we may expect the precipitation line to shift to the lower oxygen chemical potential with increasing initial A-site excess, this idea is not supported by the result of the calculation. This is mainly because the equilibrated $[V_A''']$ and $[V_B''']$ are in the percent range [Fig. 3(a), orange and green line]) due to oxygen incorporation by the Schottky reaction [Eq. (28)]. A small variation in the initial A/B ratio hardly affects

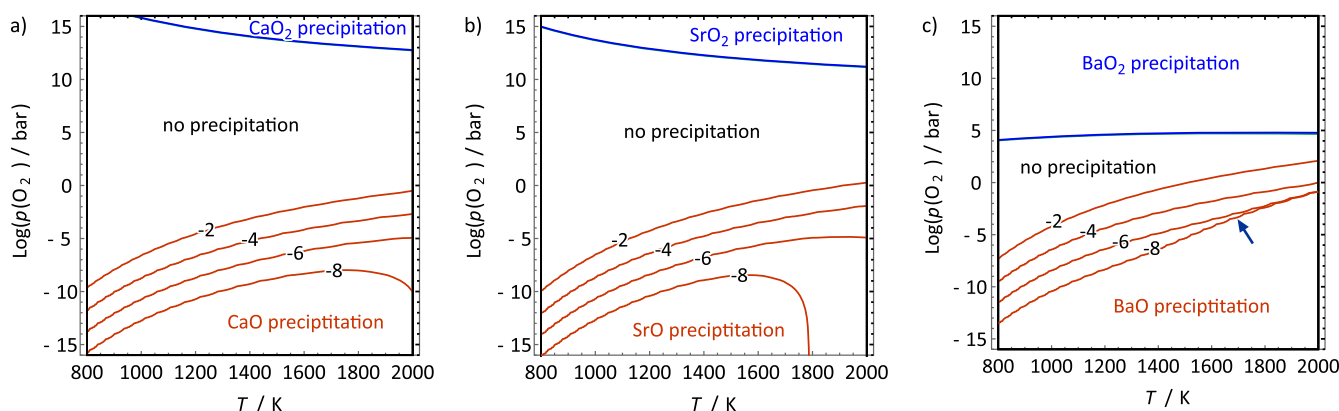
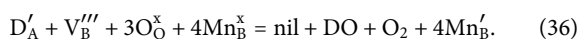


FIG. 4. Phase precipitation in LCM20 (a), LSM20 (b), and LBM20 (c) computed by equilibration of the perovskite with the dopant reservoirs, CaO_x , SrO_x , and BaO_x . Phase precipitation was calculated for different δ_{AB} at excess of A in the range of 10^{-8} to 10^{-2} , resulting in different precipitation boundaries. DO and DO_2 precipitation boundaries are shown by red and blue lines, respectively, and marked with $\log(\delta_{AB})$. The DO_2 precipitation line is not influenced by δ_{AB} ; therefore, only one blue line is visible, whereas the DO precipitation line depends strongly on δ_{AB} .

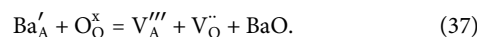
these vacancy concentrations. For further illustration, we note that the transition regime between A-site rich and A-site deficient [red and blue regions in Fig. 2(a)] is particularly narrow. From this figure, we can estimate that an initial A/B nonstoichiometry of 5% or more would be required to cause a noticeable shift of the precipitation line, assuming that the defect formation energies and entropies are unaffected by such a large nonstoichiometry. On the other hand, we observe in Fig. 4 that the dopant oxide (DO) precipitation occurs only under reducing conditions and appears to be very sensitive to the initial A/B ratio of the material. Higher A-site excess shifts the precipitation line to less reducing conditions [lower T , higher $p(\text{O}_2)$]. If oxide precipitation were to be described by a reaction similar to Eq. (35) [Eq. (11)], this reaction would be expected under oxidizing conditions and would be independent of the initial A/B ratio—contrary to our prediction. This suggests that Eq. (11) alone does not explain A-site dopant oxide precipitation from acceptor-doped LaMnO_3 . Instead, taking into account that the A-site-rich material is, in effect, doped with B-site vacancies, V_B''' , allows us to write a different precipitation reaction,



This equation can be understood as a reversal of the oxidation reaction [Eq. (9)] combined with the precipitation reaction Eq. (11). We note that this reaction is not explicitly included in our defect model; however, it can be represented as a linear combination of Eqs. (9) and (11). It is thereby implicitly considered in the defect model. For each unit of dopant oxide precipitated this way, one unit of perovskite disappears, releasing oxygen. The standard Gibbs free energy of Eq. (36) for LCM20, LSM20, and LBM20 is negative at temperatures higher than 1500 K, 1450 K, and 1150 K, respectively (cf. Fig. S4 in the [supplementary material](#)). Since (gaseous) O_2 appears only on the product side in Eq. (36) and the Mn oxidation state decreases, it is a reduction reaction that is favored under reducing conditions. Furthermore, the reaction has a positive reaction entropy (by forming gaseous O_2), making it favorable only at high temperatures. Because this reaction is driven by the release of gaseous oxygen, precipitation can be observed under reducing conditions and high temperatures.

B-site vacancies (introduced by initial A-site excess) are required for this reaction to take place, suggesting that this reaction could be suppressed by lower A-site excess or even A-site deficit. This is confirmed by the precipitation line shifting to lower $p(\text{O}_2)$ and higher temperature with decreasing δ_{AB} , as observed in Fig. 4 for all three dopants. The line eventually moves out of the region displayed in the figure for $\delta_{AB} < 10^{-11}$ for LSM20. If the calculation is initialized with B-site excess, the composition equilibrates at the same quasi-stoichiometric composition with final $\delta_{AB} \approx 10^{-11}$, implying that excess SrO will dissolve in the perovskite under reducing conditions and precipitation will not occur. For LCM20 and LBM20, the equilibrium state under reducing conditions is slightly B-site rich; however, the same conclusions apply for larger B-site excess ($>10^{-10}$). As neither of these compositions can be prepared experimentally with sub-ppm accuracy, we find that this distinction is of no practical consequence and conclude from this result that A-site deficiency will suppress precipitation under SOFC conditions.

In the case of LBM20, the precipitation curve has a slightly different shape for $\delta_{AB} = 10^{-8}$ at $T > 1400$ K [indicated by a blue arrow in Fig. 4(c)]. This feature persists even for smaller A-site excess because the equilibrated material prefers to be A-site deficient under strongly reducing conditions (cf. Fig. 3). Because our model does not consider precipitation of manganese oxides, the preference for an A-site deficit can only be explained by dopant precipitation without the assistance of B-site vacancies. This precipitation process is instead explained by the simultaneous formation of A-site vacancies and oxygen vacancies,



This reaction is not generally favored with Gibbs free energies of +3.38 eV, +3.55 eV, and +3.02 eV for LCM20, LSM20, and LBM20, respectively, at 800 K [cf. Fig. S5 in the [supplementary material](#)]. This reaction is driven only by the reaction entropy (0.024 meV, 0.111 meV, and 0.338 meV for LCM20, LSM20, and LBM20, respectively) and the configurational entropy due to the formation of cation vacancies in the perovskite. This reaction has a visible effect on the precipitation line only in the case of LBM20, where the reaction energy is the lowest and the reaction entropy is the highest. However, as this reaction is entropy-driven, its free energy is sensitive to the entropy of the dopant within the perovskite lattice. As discussed in Sec. IV, it is possible that our DFT calculations underestimate the entropy of Ba in LBM20 (Table I). As a consequence, the reaction entropy of Eq. (37) may be overestimated and its contribution to precipitation in LBM20 at high temperatures may be an artifact. This feature vanishes if $\Delta S_{\text{Ba,LBM}}$ is set to 40 J/(K mol) (cf. Fig. S6 in the [supplementary material](#)), resulting in slightly A-site rich LBM20 under reducing conditions that behaves qualitatively the same as LSM20. While we cannot say which one of these results is correct, we note that vibrational entropy can play an important role in defect chemistry and precipitation.

V. DISCUSSION

We have studied the A/B and oxygen nonstoichiometry of 20% (Ca, Sr, Ba)-doped LaMnO_3 using a DFT-based defect chemistry model. Our defect calculations model the equilibration of the doped perovskite with a dopant reservoir consisting of dopant oxide and peroxide. Both the perovskite and the dopant reservoir are equilibrated with an oxygen atmosphere. Our defect model allows us to calculate the equilibrated A/B ratio and analyze the driving forces for precipitation under oxidizing and reducing conditions. The present model does not consider surfaces explicitly. This does not imply that surface effects are insignificant in the degradation of perovskite oxide surfaces via dopant precipitation. It has been shown, including in our recent work, that perovskite oxide surfaces can be polar and support complex surface reconstructions^{29,80–83} and a wide variety of defects.²⁹ As a consequence, surfaces can exhibit different properties than the corresponding bulk structures.⁸⁴ It is particularly noteworthy that the thermodynamically stable surface termination can vary with reaction conditions and composition.^{29,85} However, we emphasize that the present calculations clearly demonstrate that there is

a bulk component to degradation (via precipitation of dopant-rich particles) as this is an inherent property of the bulk defect chemistry of nonstoichiometric acceptor-doped perovskite oxides. We believe that this acts in addition to direct surface effects. Future work can attempt to combine the contributions of surface and bulk defect chemistry in coming up with a holistic degradation model for perovskite oxide surfaces.

Under atmospheric and oxidizing conditions, acceptor-doped manganites equilibrated with a dopant reservoir prefer an A-site rich composition. Under typical preparation and calcination conditions ($T < 1800$ K in air), the equilibrated A-site excess can be in the 10^{-2} range (cf. Fig. 3). This suggests that while an A/B-stoichiometric composition may be targeted during materials synthesis, small deviations in the A/B ratio of precursors may result in a slightly nonstoichiometric perovskite because it is thermodynamically stable. On the other hand, under reducing conditions, the stable A/B ratio approaches 1, resulting in near-stoichiometric compositions. Dopant oxide precipitation occurs if A-site rich LCM20, LSM20, or LBM20 is exposed to strongly reducing conditions, such as encountered in solid oxide fuel cell (SOFC) cathodes. Precipitation under strongly oxidizing conditions (anodic polarization), on the other hand, is expected regardless of initial A/B nonstoichiometry.

Our results explain why precipitation is observed after annealing in air to sufficiently high temperatures, as well as under both anodic and cathodic polarization and ultrahigh vacuum. Experimental observations on dopant precipitation can vary quite strongly between different research groups, as a result of different sample preparation, post-treatment, and calcination, and different pulsed laser deposition (PLD) parameters (such as laser fluence or target-to-substrate distance^{63–67}). Even different samples prepared in different batches by the same protocol can yield varying results. Our finding that precipitation under reducing conditions is highly sensitive to the δ_{AB} ratio (even in the sub-ppm range) puts into perspective the large variability of surface precipitation among apparently similar experiments in the literature.^{63,67} The expected segregation and precipitation behavior may be missing entirely in films with well-adjusted or A-site deficient stoichiometries even after prolonged annealing.⁸⁰ Model studies of electrode degradation often employ thin films prepared by PLD, where the composition of the deposited film is not necessarily the same as the target composition. Since the initial composition appears so crucial for electrode degradation, it is important to know if the film is A-site rich or deficient for such studies to give clear results. The computations of the defect chemistry of doped lanthanum manganites presented in this work finally deliver a rational explanation for the wide variety of results obtained in the literature.

Unfortunately, chemical analysis is not usually able to quantify differences between major components of a material below the 10^{-3} range. However, our results are still able to help guide experiments to more reproducible results. For instance, a post-calcination treatment of an A-site rich LDM under defined reducing conditions (for instance, in a CO_2/CO mixture), followed by an acid washing step, would precipitate an initial A-site excess and remove the precipitated dopant oxide. This procedure could result in a near-stoichiometric material that would not undergo further precipitation under SOFC conditions. However, since the sensitivity of dopant precipitation to A/B nonstoichiometry is so strong, it may be impossible to

control precisely in this way. We propose instead dedicated strategies to mitigate dopant precipitation in Sec. V A.

A. Strategies to improve the stability of SOEC and SOFC electrodes

To use the new insight to improve electrode stability, we first note that the driving force for dopant precipitation, in the framework of point defect reactions, is different in the oxidizing (SOEC) and the reducing (SOFC) regime. In both regimes, compounds are formed by endothermic reactions (indicated by positive reaction energies in Table II). In both cases, precipitation is driven by entropy rather than energy. Oxygen uptake and loss are the decisive factors in both regimes. Oxygen uptake and loss are essentially limited by the number of redox-active sites, i.e., the concentrations of Mn^{2+} , Mn^{3+} , and Mn^{4+} . Under anodic polarization (SOEC), precipitation of a peroxide allows the solid phases to bind more oxygen per Mn^{4+} (1 O/Mn) compared to the Schottky reaction (1/2 O/Mn). Therefore, this reaction is highly favorable under anodic polarization despite the formation of an unstable compound. Under cathodic polarization (SOFC), it is favorable to transfer oxygen from the solid phases into the gas phase. However, precipitation by Eq. (1) requires oxygen uptake, which is unfavorable under these conditions because of high temperature and the low oxygen chemical potential. Only with a small amount of A-site excess, precipitation can become a net oxygen loss reaction [Eq. (36)] that is favorable under reducing conditions. We suggest different strategies to improve the stabilities of SOEC and SOFC electrodes based on our results.

For SOEC electrodes, our results clearly show that the precipitation onset shifts to higher $p(\text{O}_2)$ for smaller A-site dopant cations, that is, LCM20 is the most stable of the three materials under anodic polarization. This trend is in good agreement with polarization studies on thin films³⁰ and is traced back to two properties: lower chemical potential (higher stability) of the dopant cation, Ca^{2+} , dissolved in LaMnO_3 and lower stability of the dopant peroxide CaO_2 compared to SrO_2 and BaO_2 . The stability trends are reversed: dopants dissolved in LaMnO_3 become less strongly bound (with respect to the dopant oxide) along the Ca, Sr, Ba series. The peroxide, on the other hand, becomes more stable along the Ca, Sr, Ba series. Consequentially, smaller dopants will make the SOEC electrode more stable under oxidizing conditions. Unfortunately, A-site dopants smaller than Ca^{2+} , such as Mg^{2+} , cannot be employed in manganites because they prefer to occupy the B-site.^{86–88} Another option to tackle this problem would be to increase the binding energy of Ca^{2+} within the perovskite. This could be achieved, in principle, by doping either the A-site or the B-site while not deteriorating the properties of the active electrode material. B-site doping is likely to alter the material's electronic properties and perhaps the defect chemistry altogether. Another option would be doping the A-site with another 2+ or 3+ dopant ($\text{La}_{0.8-x}\text{Ca}_{0.2}\text{A}_x\text{MnO}_3$). Since all possible 2+ dopant candidates (Sr and Ba) are more prone to precipitation than Ca, they are not a promising option. However, it is worth to visit the rare earth elements to assess if they present the desired effect of increasing the binding energy of the A-site dopants in the perovskite.

In the reducing (SOFC) range, we observe almost no difference between the three dopants regarding oxide precipitation, despite

large differences in reducibility of the (Ca, Sr, Ba)-doped manganites. However, we find dopant precipitation to be promoted by increasing the initial A/B ratio, while A-site deficiency suppresses precipitation. Precipitation under reducing conditions could therefore be mitigated by employing compositions with B-site excess. This trend has been demonstrated qualitatively by thin film studies employing 5% A-site deficient and A/B stoichiometric PLD targets.⁸⁹ The films deposited from the A-site deficient target showed less precipitation and less total Sr surface enrichment after annealing than the films deposited from the stoichiometric targets.⁸⁹ Unfortunately, this trend has not yet been demonstrated for powder samples or high-surface-area materials. A-site deficient materials are already employed in SOFC applications for a different reason, that is, suppressing the formation of the lanthanum zirconate pyrochlore $\text{La}_2\text{Zr}_2\text{O}_7$ phase at the LSM/YSZ interface⁴⁶ during SOFC operation. It is well-established that Sr is enriched near the surface during electrode deactivation⁹⁰ even for the A-site deficient LSM20. However, it is uncertain if SrO precipitation occurs in A-site deficient LSM20 electrodes or if the observed surface enrichment is rather a result of the formation of a SrO monolayer or Sr enrichment (La/A-site vacancy depletion) within the perovskite lattice, both of which appear to be unrelated to phase precipitation.²⁹ This means that one phenomenon can arise without the other because they have fundamentally different driving forces, although they occur under similar conditions in the SOFC operating range. While Sr enrichment near the surface and a change of surface termination are driven by a reduction in the surface dipole moment, phase precipitation is driven by the bulk defect chemistry. While the precipitates usually appear on the surface, we find the surface not responsible for their emergence. In this context, it is worth noting that it is still unclear if the experimentally observed degradation of electrode activity is mainly due to the formation of Sr-rich precipitates, the resulting changes in the cation, anion, and electronic defects within the lattice, Sr enrichment in the bulk lattice near the surface, the formation of a SrO mono- or semi-layer, or due to a combination of these processes.^{23,27–29,91} This further highlights the necessity for dedicated model experiments focusing on the surface chemistry and atomic structure of perovskite oxides.^{13,24,80–83,92–94}

VI. SUMMARY AND CONCLUSION

We have expanded the defect model for 20% acceptor-doped (Ca, Sr, Ba) LaMnO_3 by equilibration of the bulk material with a dopant oxide/peroxide reservoir to account for dopant dissolution and precipitation. Energies and entropies of defect reactions are entirely derived from density functional theory calculations. This model allows us to include the role of defect chemistry in explaining the driving forces of dopant precipitation under oxidizing (SOEC) and reducing (SOFC) conditions, in addition to our earlier work revealing the electrostatic and elastic energy contributions to dopant segregation on perovskite oxides.^{15,30} Having established this model, we have assessed the role of different dopant sizes and initial A/B ratios on the precipitation of dopant oxides under conditions of anodic and cathodic polarization.

We find that the doped LaMnO_3 equilibrated with the dopant reservoir prefers a highly A-site rich composition at atmospheric [$p(\text{O}_2) \approx 1$ bar] and oxidizing [$p(\text{O}_2) > 1$ bar] conditions. The

doped lanthanum manganites appear to support large variations in the A/B ratio under typical calcination conditions. Under reducing (SOFC) conditions and high temperatures, the equilibrated A/B ratio is near-stoichiometric with a small A-site (LSM20) or B-site (LCM20, LBM20) excess in the sub-ppb range. Under strongly oxidizing (SOEC) conditions, we find the stable composition to be A-site deficient.

Precipitation phase boundaries were calculated for a large range of initial A-site excess ($10^{-8} \leq \delta_{\text{AB},0} \leq 10^{-2}$), and precipitation was obtained under both SOEC (strongly oxidizing) and SOFC (strongly reducing) conditions. Under SOEC conditions, precipitation is driven by oxygen uptake by the solid phase, forming dopant peroxide and large concentrations of A-site vacancies. This results in an A-site deficiency within the perovskite bulk. The precipitation boundary under SOEC conditions is found to be insensitive to the initial A/B ratio. However, a shift to lower $p(\text{O}_2)$ and lower temperature is observed within the dopant series from Ca to Sr to Ba, indicating that LCM20 is expected to be the most stable material under oxidizing conditions as required, for example, in SOEC anodes. In contrast, the precipitation boundary under SOFC (strongly reducing) conditions is not influenced by the dopant size, but is very sensitive to the initial A-site excess. Increasing the initial A-site excess shifts the precipitation boundary to higher $p(\text{O}_2)$ and lower temperature. This indicates decreased stability of the cathode material with increased A-site excess in an SOFC. The driving force for precipitation under reducing conditions was found to be the release of oxygen from the condensed phase into the atmosphere, which can be accompanied by dopant oxide precipitation only if the material is initially A-site rich.

Our defect model for doped lanthanum manganites, including the exchange of dopant cations with a reservoir, gives new insights about the connection between dopant precipitation and the dopant size, material composition, and operating conditions. Examining the driving forces for precipitation under SOEC and SOFC operating conditions allows us to propose material design strategies to improve electrode stability.

SUPPLEMENTARY MATERIAL

See the [supplementary material](#) for the equilibrated activities of dopant reservoirs, justification of assumption, comparison between a defect model with and without dopant equilibration, equilibrated defect concentrations, standard free energy of Schottky-like precipitation, standard free energy of pure precipitation, precipitation diagram for LBM20 using two different entropies, and precipitation diagram for LSM20 with and without entropy.

ACKNOWLEDGMENTS

We thank the German Research Foundation (DFG Project No. 324830457) and Fonds der Chemischen Industrie for a fellowship for Franziska Hess and the MIT Energy Initiative for supplementary funding. This project would not have been possible without the computation time allocated by XSEDE (Grant No. TG-DMR120025) and NERSC (Contract No. DE-AC02-05CH11231) on the Stampede2 and Cori high performance computing clusters. We gratefully

acknowledge the staff at TACC, NERSC, and MGHPCC for technical support.

DATA AVAILABILITY

The data that support the findings of this study are available within the article and its [supplementary material](#).

REFERENCES

- ¹D. M. Smyth, *Annu. Rev. Mater. Sci.* **15**, 329 (1985).
- ²M. Kubicek, A. H. Bork, and J. L. M. Rupp, *J. Mater. Chem. A* **5**, 11983 (2017).
- ³M. A. Peña and J. L. G. Fierro, *Chem. Rev.* **101**, 1981 (2001).
- ⁴H. Zhu, P. Zhang, and S. Dai, *ACS Catal.* **5**, 6370 (2015).
- ⁵J. Hwang *et al.*, *Science* **358**, 751 (2017).
- ⁶F. Polo-Garzon and Z. Wu, *J. Mater. Chem. A* **6**, 2877 (2018).
- ⁷C. N. R. Rao and S. Dey, *J. Solid State Chem.* **242**, 107 (2016).
- ⁸C. Agrafiotis, M. Roeb, and C. Sattler, *Renewable Sustainable Energy Rev.* **42**, 254 (2015).
- ⁹J. R. Scheffe and A. Steinfeld, *Mater. Today* **17**, 341 (2014).
- ¹⁰L. Malavasi, C. A. J. Fisher, and M. S. Islam, *Chem. Soc. Rev.* **39**, 4370 (2010).
- ¹¹E. C. C. de Souza and R. Muccillo, *Mater. Res.* **13**, 385 (2010).
- ¹²B. Han *et al.*, *Phys. Chem. Chem. Phys.* **17**, 22576 (2015).
- ¹³Z. Feng *et al.*, *Acc. Chem. Res.* **49**, 966 (2016).
- ¹⁴M. Niania *et al.*, *J. Mater. Chem. A* **6**, 14120 (2018).
- ¹⁵W. Lee, J. W. Han, Y. Chen, Z. Cai, and B. Yildiz, *J. Am. Chem. Soc.* **135**, 7909 (2013).
- ¹⁶J. Druce *et al.*, *Energy Environ. Sci.* **7**, 3593 (2014).
- ¹⁷J. Druce, T. Ishihara, and J. Kilner, *Solid State Ionics* **262**, 893 (2014).
- ¹⁸T. T. Fister *et al.*, *Appl. Phys. Lett.* **93**, 151904 (2008).
- ¹⁹W. Harrison, *Phys. Rev. B* **83**, 155437 (2011).
- ²⁰M. M. Kukulja, Y. A. Mastrikov, B. Jansang, and E. A. Kotomin, *J. Phys. Chem. C* **116**, 18605 (2012).
- ²¹A. S. Raman, R. Patel, and A. Vojvodic, "Surface stability of perovskite oxides under OER operating conditions: A first principles approach," *Faraday Discuss.* (published online) (2020).
- ²²N. Tsvetkov, Q. Lu, L. Sun, E. J. Crumlin, and B. Yildiz, *Nat. Mater.* **15**, 1010 (2016).
- ²³Y. A. Mastrikov, R. Merkle, E. A. Kotomin, M. M. Kukulja, and J. Maier, *J. Mater. Chem. A* **6**, 11929 (2018).
- ²⁴J. M. P. Martinez *et al.*, *J. Am. Chem. Soc.* **137**, 2939 (2015).
- ²⁵T. Akbay *et al.*, *J. Mater. Chem. A* **4**, 13113 (2016).
- ²⁶A. Staykov *et al.*, *Chem. Mater.* **27**, 8273 (2015).
- ²⁷Y. Cheng *et al.*, *J. Phys. Chem. Lett.* **10**(14), 4082 (2019).
- ²⁸A. Staykov *et al.*, *Sci. Technol. Adv. Mater.* **19**, 221 (2018).
- ²⁹F. Hess and B. Yildiz, *Phys. Rev. Mater.* **4**, 015801 (2020).
- ³⁰D. Kim, R. Bliem, F. Hess, J.-J. Gallet, and B. Yildiz, *J. Am. Chem. Soc.* **142**, 3548 (2020).
- ³¹J. Mizusaki *et al.*, *Solid State Ionics* **129**, 163 (2000).
- ³²Y.-L. Lee and D. Morgan, *Phys. Chem. Chem. Phys.* **14**, 290 (2012).
- ³³R. Meyer, R. Waser, J. Helmbold, and G. Borchardt, *J. Electroceram.* **9**, 101 (2002).
- ³⁴J. Mizusaki, S. Yamauchi, K. Fueki, and A. Ishikawa, *Solid State Ionics* **12**, 119 (1984).
- ³⁵J. Mizusaki, M. Yoshihiro, S. Yamauchi, and K. Fueki, *J. Solid State Chem.* **58**, 257 (1985).
- ³⁶J. Mizusaki, Y. Mima, S. Yamauchi, K. Fueki, and H. Tagawa, *J. Solid State Chem.* **80**, 102 (1989).
- ³⁷S. Carter *et al.*, *Solid State Ionics* **53-56**, 597 (1992).
- ³⁸J. Mizusaki, *Solid State Ionics* **52**, 79 (1992).
- ³⁹F. Hess, A. Staykov, B. Yildiz, and J. Kilner, "Chapter: Solid oxide fuel cell materials and interfaces," in *Handbook of Materials Modeling* (Springer, Cham, 2019).
- ⁴⁰J. Nowotny and M. Rekas, *J. Am. Ceram. Soc.* **81**, 67 (1998).
- ⁴¹J. H. Kuo, H. U. Anderson, and D. M. Sparlin, *J. Solid State Chem.* **83**, 52 (1989).
- ⁴²J. A. M. van Roosmalen and E. H. P. Cordfunke, *J. Solid State Chem.* **110**, 113 (1994).
- ⁴³D. Mebane, Y. Liu, and M. Liu, *Solid State Ionics* **178**, 1950 (2008).
- ⁴⁴M. Takacs *et al.*, *Acta Mater.* **103**, 700 (2016).
- ⁴⁵A. Y. Zuev and D. S. Tsvetkov, *Solid State Ionics* **181**, 557 (2010).
- ⁴⁶S. Jiang *et al.*, *Solid State Ionics* **121**, 1 (1999).
- ⁴⁷D. Neagu, G. Tsekouras, D. N. Miller, H. Ménard, and J. T. S. Irvine, *Nat. Chem.* **5**, 916 (2013).
- ⁴⁸L. Sun, D. Marrocchelli, and B. Yildiz, *Nat. Commun.* **6**, 6294 (2015).
- ⁴⁹H. Tanaka *et al.*, *Angew. Chem., Int. Ed.* **45**, 5998 (2006).
- ⁵⁰D. Papargyriou, D. N. Miller, and J. T. S. Irvine, *J. Mater. Chem. A* **7**, 15812 (2019).
- ⁵¹Y. Gao, D. Chen, M. Saccoccio, Z. Lu, and F. Ciucci, *Nano Energy* **27**, 499 (2016).
- ⁵²G. Yang, W. Zhou, M. Liu, and Z. Shao, *ACS Appl. Mater. Interfaces* **8**, 35308 (2016).
- ⁵³Y. Takeda *et al.*, *Mater. Res. Bull.* **26**, 153 (1991).
- ⁵⁴Y. Zuo, J. Li, J. Yi, Z. Wang, and C. Chen, *J. Solid State Chem.* **181**, 700 (2008).
- ⁵⁵J. A. M. van Roosmalen, P. van Vlaanderen, E. H. P. Cordfunke, W. L. IJdo, and D. J. W. IJdo, *J. Solid State Chem.* **114**, 516 (1995).
- ⁵⁶V. A. Khomchenko, I. O. Troyanchuk, and H. Szymczak, *Mater. Chem. Phys.* **111**, 154 (2008).
- ⁵⁷A. Feldhoff, J. Martynczuk, and H. Wang, *Prog. Solid State Chem.* **35**, 339 (2007).
- ⁵⁸M. Mori *et al.*, *J. Electrochem. Energy Convers. Storage* **8**, 051014 (2011).
- ⁵⁹F. Gao *et al.*, *J. Power Sources* **185**, 26 (2008).
- ⁶⁰L. Zhang *et al.*, *Int. J. Hydrogen Energy* **43**, 3761 (2018).
- ⁶¹F. Morin, G. Trudel, and Y. Denos, *Solid State Ionics* **96**, 129 (1997).
- ⁶²M. Sogaard, P. V. Hendriksen, F. W. Poulsen, and M. Mogensen, *J. Electroceram.* **13**, 811 (2004).
- ⁶³S. Wicklein *et al.*, *Appl. Phys. Lett.* **101**, 131601 (2012).
- ⁶⁴D. J. Keeble *et al.*, *Phys. Rev. Lett.* **105**, 226102 (2010).
- ⁶⁵D. Kan and Y. Shimakawa, *Appl. Phys. Lett.* **99**, 081907 (2011).
- ⁶⁶E. Breckenfeld *et al.*, *Chem. Mater.* **24**, 331 (2012).
- ⁶⁷P. Orgiani, R. Ciancio, A. Galdi, S. Amoroso, and L. Maritato, *Appl. Phys. Lett.* **96**, 032501 (2010).
- ⁶⁸G. Kresse and J. Furthmüller, *Phys. Rev. B* **54**, 11169 (1996).
- ⁶⁹G. Kresse and D. Joubert, *Phys. Rev. B* **59**, 1758 (1999).
- ⁷⁰J. P. Perdew *et al.*, *Phys. Rev. B* **46**, 6671 (1992).
- ⁷¹S. L. Dudarev, G. A. Botton, S. Y. Savrasov, C. J. Humphreys, and A. P. Sutton, *Phys. Rev. B* **57**, 1505 (1998).
- ⁷²Y. Tokura and Y. Tomioka, *J. Magn. Magn. Mater.* **200**, 1 (1999).
- ⁷³L. Wang, T. Maxisch, and G. Ceder, *Phys. Rev. B* **73**, 195107 (2006).
- ⁷⁴J. Rodríguez-Carvajal *et al.*, *Phys. Rev. B* **57**, R3189 (1998).
- ⁷⁵Landolt-Bornstein Database, Springer Materials, 2010.
- ⁷⁶L. Rørmøk, K. Wiik, S. Stølen, and T. Grande, *J. Mater. Chem.* **12**, 1058 (2002).
- ⁷⁷A. G. Bhavani, W. Y. Kim, and J. S. Lee, *ACS Catal.* **3**, 1537 (2013).
- ⁷⁸S. C. Middleburgh, K. P. D. Lagerlof, and R. W. Grimes, *J. Am. Chem. Soc.* **96**, 308 (2013).
- ⁷⁹Y. Chen *et al.*, *Chem. Mater.* **27**, 5436 (2015).
- ⁸⁰G. Franceschi, M. Schmid, U. Diebold, and M. Riva, *J. Mater. Chem. A* **8**, 22947 (2020).
- ⁸¹M. Setvin *et al.*, *Science* **359**, 572 (2018).
- ⁸²M. Riva *et al.*, *Nat. Commun.* **9**, 3710 (2018).
- ⁸³S. Gerhold, Z. Wang, M. Schmid, and U. Diebold, *Surf. Sci.* **621**, L1 (2014).
- ⁸⁴S. Piskunov, E. Spohr, T. Jacob, E. Kotomin, and D. Ellis, *Phys. Rev. B* **76**, 012410 (2007).

- ⁸⁵S. Piskunov *et al.*, [Phys. Rev. B](#) **78**, 121406 (2008).
- ⁸⁶P. Somasundaram *et al.*, [S. Afr. J. Chem. Eng.](#) **23**, 50 (2017).
- ⁸⁷A. Maignan and B. Raveau, [Z. Phys. B: Condens. Matter](#) **102**, 299 (1997).
- ⁸⁸I. O. Troyanchuk, M. V. Bushinsky, H. Szymczak, K. Bärner, and A. Maignan, [Eur. Phys. J. B](#) **28**, 75 (2002).
- ⁸⁹W. Lee and B. Yildiz, [ECS Trans.](#) **57**, 2115 (2013).
- ⁹⁰S. P. Jiang, [J. Solid State Electrochem.](#) **11**, 93 (2007).
- ⁹¹Y. Cao, M. J. Gadre, A. Ngo, S. B. Adler, and D. D. Morgan, [Nat. Commun.](#) **10**, 1346 (2019).
- ⁹²E. H. Morales, J. M. P. Martirez, W. A. Saidi, A. M. Rappe, and D. A. Bonnell, [ACS Nano](#) **8**, 4465 (2014).
- ⁹³W. Jung and H. L. Tuller, [Energy Environ. Sci.](#) **5**, 5370 (2012).
- ⁹⁴M. Kubicek, A. Limbeck, T. Frömling, H. Hutter, and J. Fleig, [J. Electrochem. Soc.](#) **158**, B727 (2011).